Low-intensity magnetic fields induce anomalous disorder-to-order transition in spherical block copolymer micelle solutions

Grace V. Kresge, Christopher A. P. Neal, and Michelle A. Calabrese*

Department of Chemical Engineering & Materials Science, University of Minnesota, Minneapolis, MN, 55455, USA

E-mail: mcalab@umn.edu

Phone: +1 612 625 2551

TOC Graphic

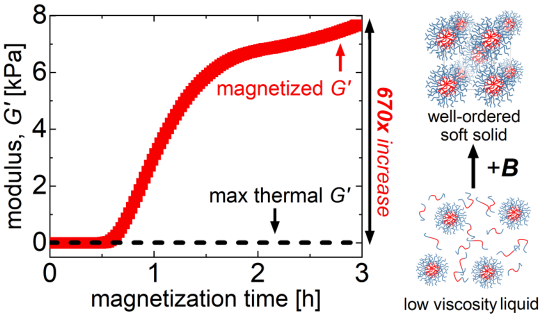

Abstract

Magnetic field processing is promising for directing and enhancing self-assembly of diamagnetic block copolymers (BCPs) via domain *alignment*, but is typically limited to high field strengths and few polymer chemistries. Herein, a novel magnetic field-induced ordering mechanism distinct from domain alignment is demonstrated in aqueous, spherical BCP micelles. Here, low-intensity magnetic fields ($B \leq 0.5$ T) induce an anomalous disorder-to-order transition, accompanied by a several order-of-magnitude increase in shear modulus– effectively transforming a low viscosity liquid into an ordered soft solid. The induced moduli are orders of magnitude larger than those resulting from thermally-induced ordering. Further magnetization induces cubic-to-cylinder order-to-order transitions. Comprehensive characterization via magnetorheology, small- and wide-angle X-ray scattering, differential scanning calorimetry, and vibrational spectroscopy reveals a significant reduction in micelle size and aggregation number relative to zero-field temperature- or concentration-induced ordering, suggesting that ***B***-fields strongly alter polymer-solvent interactions. This extraordinary BCP ordering strategy enables discovery of structures and *d*-spacings inaccessible via traditional processing routes, thus providing a new platform for developing advanced materials with precisely-controlled features.

Introduction

Amphiphilic block copolymers (BCPs) are attractive for designing functional materials, as their self-assembly and properties are tunable via amphiphile chemistry, composition, shape, and chain length. Analogous to small-molecule surfactant lyotropic liquid crystals (LCs), aqueous BCPs self-assemble into domains of spherical, cylindrical and lamellar packings. These chemically diverse soft materials offer exceptional advances in applications ranging from templates for nanomaterials synthesis,[1,2] drug delivery devices,[3] selective transport membranes,[4,5] lithography[6] and information storage media.[7,8] However, reliable methods for processing BCPs with controlled phase dimensions, grain size, and orientation remain challenging, limiting their practical utility. External field processing, including shear,[9,10] electric fields[11,12] and magnetic fields,[13–16] offers diverse routes to control the organization of soft materials at the molecular and mesoscopic level. Enhanced grain size and orientation can be achieved by shear and electric fields, but these methods challenge the stability of polymer matrices.[17–21] Electric field processing is typically limited to a few polymer chemistries, thin samples, and high field intensities.[18–21] Alternatively, magnetic fields are non-damaging and can be applied over long length scales[22] and in complex geometries.[23]

Magnetic field-directed assembly of soft materials to date has focused on controlling *domain alignment* (**Scheme 1**), via aligning anisotropic mesostructures like rods or lamellae, enhancing ordering of lamellar (*lam*) or hexagonal (*cyl*) phases, and tuning phase orientation angle via organic additives or rotational annealing.[16,24–26] Near phase boundaries, this domain alignment can cause minor changes in the order-to-order transition (OOT) or order-to-disorder transition (ODT) temperatures.[13] Additionally, disorder-to-order (DOT) transitions to aligned diamagnetic BCP phases like *cyl* and *lam* can be induced by adding magnetite nanoparticles and processing both thermally and magnetically.[27] For axis-symmetric diamagnetic materials like most polymers and surfactants, the driving force for domain alignment is the magnetostatic energy originating from anisotropy in the magnetic susceptibility, $\Delta\chi$.[28] In BCPs, $\Delta\chi$ can arise from a difference in χ between blocks A and B ($\chi_A \neq \chi_B$), or from collective anisotropic magnetic susceptibilities of chains in an anisotropic BCP domain, taken along and perpendicular to the axis of highest rotational symmetry ($\chi_{\parallel} \neq \chi_{\perp}$).[29]

For magnetic field alignment, the orientation-dependent contribution to the magnetostatic energy must exceed thermal energy:[30–33] $-\Delta\chi \boldsymbol{B}^2 V_g/2\mu_0 \gg k_B T$ (**Eq. 1**), where $\boldsymbol{B}$ is the magnetic flux density, μ_0 is the permeability of free space, and V_g is the grain volume. While a wide array of soft, polymeric, and biological materials have been aligned in $\boldsymbol{B}$-fields,[15,16,34,35] this technique is challenging to employ as many soft materials have low $\Delta\chi$. Thus, magnetic field alignment of diamagnetic BCPs typically requires large field strengths,[13,14,28,36] addition of LC,[16] semi-crystalline,[15,37] or rod-like blocks,[13,14,16,28,31] substantial chain anisotropy,[28] or combinations thereof.[38]

Here, we present a novel magnetic field-induced ordering mechanism – distinct from domain alignment – in diamagnetic, geometrically-isotropic spherical BCP micelles ($\chi_{\parallel} = \chi_{\perp}$) with poor chain susceptibility contrast ($\chi_A \approx \chi_B$) formed from triblock copolymers composed of polyethylene oxide (PEO) endblocks and a polypropylene oxide (PPO) midblock (**Scheme 1**). Previously, field-induced alignment of spherical particles into anisotropic, chain-like structures has only been observed in ferro- and paramagnetic particles, due to dipole alignment. Here, however, ordered soft solids form rapidly upon application of weak magnetic fields ($\boldsymbol{B} \leq 0.5$ T) to low viscosity solutions of randomly-distributed micelles in the fluid state far from known phase boundaries, resulting in up to a six-order of magnitude increase in the dynamic moduli that persists upon field removal. As initial micelles are disordered and isotropic, and the anisotropic magnetic susceptibilities of individual chains in the micelle collectively average to zero, domain alignment is not the primary driver of this induced ordering. However, this ***B***-induced phase creation yields ordered phases classically observed with increasing temperature or concentration, suggesting that low-intensity magnetic fields primarily modify polymer-solvent interactions, which in turn alter self-assembly. Systematic evaluation of the initial DOT and subsequent OOTs via magnetorheology (MR), small- and wide-angle X-ray scattering (SAXS/WAXS), differential scanning calorimetry (DSC), and vibrational spectroscopy strongly supports this hypothesis, revealing significant enhancement in the mechanical properties and a reduction in micelle aggregation number relative to zero-field temperature- or concentration-induced ordering. This novel assembly mechanism reveals how magnetic fields can be harnessed to control polymer conformation, self-assembly, and ordering via mechanisms distinct from field-induced alignment, providing a promising route for rationally designing advanced materials.

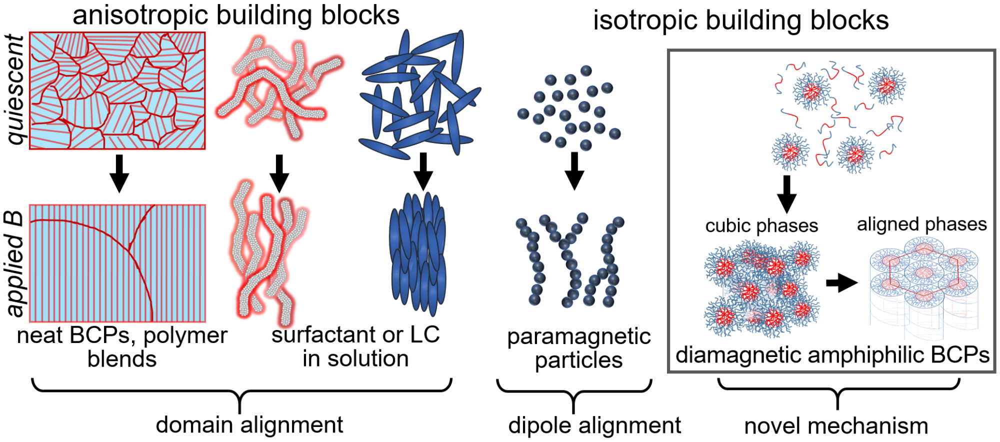

Scheme 1: Magnetic field (***B***)-induced material responses. (L) Prior work on diamagnetic materials involves alignment of anisotropic constituents (wormlike micelles, liquid crystals) and phases (lamellae, cylinders); isotropic paramagnetic particles can form chains due to ***B***-induced dipole alignment. (R) In contrast, this work demonstrates ***B***-induced ordering in diamagnetic, isotropic building blocks into both isotropic and aligned phases.

Materials and Methods

Materials

Magnetically-induced ordering transitions were examined in triblock polymers known as poloxamers, of the architecture poly(ethylene oxide)-poly(propylene oxide)-poly(ethylene oxide) (PEO-

PPO-PEO). The primary experiments were conducted on poloxamer 333 (P333) and poloxamer 335 (P335), with supplementary experiments performed on poloxamer 407 (P407). Poloxamer number-average molecular weights, M_n ranged from 5 to 12.6 kDa (see **Section S2.2** for size exclusion chromatography) with PEO weight fractions from x_{PEO} = 0.3 to 0.7 (see NMR analysis in **Section S2.1**). For P333, $M_n \approx 5$ kDa and $w_{PEO} \approx 0.3$; for P335, $M_n \approx 6.5$ kDa and $w_{PEO} \approx 0.5$; for P407, $M_n \approx 12.6$ kDa and $w_{PEO} \approx 0.7$.

All materials were used as received. P333 and P335 were obtained from BASF and P407 from Sigma-Aldrich. PEO ($M_n \approx 3.4$ kDa), PPO ($M_n \approx 4$ kDa), and deuterium oxide (99.9%) were purchased from Sigma-Aldrich. Polymer solutions were prepared at 20% wt in HPLC-grade water in clean glass vials. To dissolve the polymer in water, samples were refrigerated on a shaker at 4 °C for 2 days. Samples were mixed again at room temperature by vortexing prior to each experiment. A similar procedure was followed for samples in deuterium oxide (D_2O), which was done for small angle neutron scattering (SANS).

Rheometry

Zero-field rheology and magnetorheology measurements were performed on an Anton Paar MCR 702 rheometer using a 20 mm parallel plate geometry. For all oscillatory time sweeps, the material response was monitored at 20 °C and a 1 rad·s^{-1} frequency and an amplitude of 0.5%, which is at or near the linear viscoelastic regime.

Magnetorheology: MR was performed using the Anton Paar magneto-rheological device (MRD); for additional details on the MRD setup and protocols, see **Section S1.1**. Briefly, this device consists of an electro-magnet located under the bottom plate and a magnetic yolk which encloses the geometry. A Teslameter (Magnet-Physik FH54) combined with Hall probe, fitted below the inset plate, measured the magnetic flux density, $\boldsymbol{B}$, acting on the sample. The gap between the measuring plates was fixed at 1 mm and was unaffected by the applied field. Temperature control was maintained via coolant (ethylene glycol-water 50:50 mixture) circulation, and manipulated through a programmable controller (Omega, Stamford, CT). Extensive calibrations were done to counteract inductive heating from the electromagnet, which are detailed further in **Section S1.1** and Ref. 39.

For each experiment, a fixed volume (0.8 mL) of cold sample was loaded onto the inset plate. After the upper plate reached the operating gap, the plates were covered with the MRD yoke, and the sample was allowed to equilibrate for ten minutes prior to initiating time sweeps. For each poloxamer, time sweeps for a control at 0 T were measured for the same duration as the magnetization time to confirm that no change in the rheological properties occurred.

Zero-field rheology: In this article, 'zero-field' refers to measurements performed without applied magnetic field, i.e., at 0 T. To determine the zero-field rheological behavior of each poloxamer, oscillatory time sweeps at 20 °C and oscillatory temperature ramps were performed. Oscillatory time sweep controls were performed using the same setup, geometry, and temperature control for MR, as described above. Oscillatory temperature ramps were performed using the same parallel plate geometry, but temperature was instead controlled using the Anton Paar H-PTD200 Peltier device affixed with an evaporation blocker. Temperature was increased from 5 °C to at least 55 °C at a heating rate of 1 $°C{\cdot}min^{-1}$. Samples were equilibrated at 5 °C for 10 minutes prior to temperature ramp experiments. The material response was monitored at 1 $rad{\cdot}s^{-1}$ frequency and at constant amplitude of 0.5%.

Small angle x-ray scattering (SAXS)

Lab source SAXS was performed at the Characterization Facility, University of Minnesota using a SAXSLAB Ganesha 300XL instrument. Cu Kα x-rays (λ = 1.54 Å) generated by a Xenocs Geni3DX source were collimated through 2 sets of 4-bladed slits (JJ X-ray, A/S). 2D-SAXS patterns were acquired using a EIGER R 1M Dectris detector (7.72 cm × 7.99 cm rectangular area) with 1030 × 1065 pixels (75 μm × 75 μm pixel size) at a sample-to-detector distance of 46.8 cm and a wave vector, q, covering q = 0.02 – 0.7 Å^{-1}. SAXS diffractograms were calibrated using a silver behenate standard with d-spacing of 58.38 Å. All 2D-SAXS patterns were azimuthally-integrated to obtain the 1D scattering intensity, using the DataSqueeze software. The 1D scattering intensities were analyzed using customized Igor Pro procedure files and SASfit software. The micelle radius, R_t, in cubic ordered phases was estimated as half the nearest neighbor distance. Details about the core-shell fitting routine for SAXS and SANS data can be found in references 40- 41, and are summarized in **Section S9.1**.

Small angle x-ray scattering (SAXS) acquisition on magnetized poloxamers was started within 30 minutes of ending MR experiments. Experiments were performed at ambient conditions to minimally disrupt the induced microstructure, $T = 22 \pm 1$ ° C. Samples were collected from the rheometer and subsequently sealed between two Kapton sheets with an o-ring in sample holders. Sample holders were then mounted within an evacuated sample chamber at ambient conditions. As samples often required long magnetization times and had to be measured immediately following MR, most SAXS measurements had to be performed in-house vs. at a synchrotron facility. For additional details regarding the in-house SAXS set up and supplemental data, see **Section S1.4**.

Fourier-transform infrared (FTIR) spectroscopy

FTIR spectra were measured using a Thermo Nicolet 6700 spectrometer with a diamond crystal in attenuated total reflection (ATR) mode with 0.964 cm^{-1} resolution from 840 cm^{-1} to 4000 cm^{-1}; 64 scans were obtained for each spectrum. IR spectra were baseline corrected using a 5 factor polynomial fit through the ThermoFisher OMNIC software. Measurements were performed under vacuum to eliminate minor spectral contributions due to residual water vapor; a smoothing correction for atmospheric water background was performed. FTIR was performed immediately following magnetization at 0.5 T at 20 °C. For details about FTIR deconvolution and analysis, see **Section S7.1**.

Results

Magnetic field induces anomalous disorder-to-cubic transition in P335

When exposed to low-intensity magnetic fields at 20 °C, aqueous solutions of the PEO-PPO-PEO triblock poloxamer P335 (20% wt) exhibit an anomalous disorder-to-order phase transition (DOT), detected in magnetorheology via a four-orders of magnitude increase in the dynamic moduli, G' and G'' (**Fig. 1**). Poloxamer 335 has a PEO weight fraction, w_{PEO}, of ~50% and a number-average molecular weight, $M_{n,P335}$, of 6.5 kDa (**Figs. S1-S3**). The classic field-induced domain alignment mechanism for diamagnetic block copolymers (BCPs) (**Scheme 1**) is insufficient to explain this transition given the low field intensity and low magnetic susceptibility anisotropy associated with this system (**Eq. 1**). Here, volume magnetic susceptibilities of the individual blocks are similar ($\chi_{PEO} = -8.8 \cdot 10^{-6}$, $\chi_{PPO} = -8.6 \cdot 10^{-6}$), resulting in a low chain susceptibility anisotropy ($\Delta\chi \sim 10^{-10}$, **Section S3.5**), and $\Delta\chi$ of the disordered micelle phase averages to approximately zero due to the spherical shape (**Fig. 1a**). Further, superconducting quantum interference device (SQUID), vibrating sample magnetometer (VSM), and inductively coupled plasma-optical emission spectrometry (ICP-OES) measurements confirm that poloxamer solutions are diamagnetic, and free of impurities with high magnetic susceptibility (**Figs. 1b, S3, S9**); see **Section S1** for *Methods*. Magnetic hysteresis loops of aqueous poloxamers exhibit no net magnetic hysteresis and a negative slope in the magnetic moment vs. magnetic flux density ($\boldsymbol{B}$) yielding a small negative magnetic susceptibility, characteristic of diamagnetism (**Fig. 1b**). The magnetically-induced ordering transition described within is also robust to salt impurities (**Fig. S4**), polymer batch-to-batch variation (**Fig. S5**), and homopolymer and diblock impurities (**Figs. S7, S8**).

Small-angle X-ray scattering (SAXS) confirms that at ambient conditions prior to MR, these P335 solutions consist of disordered (*dis*), spherical micelles (**Fig. 1d**), as indicated by the two broad peaks in the 2D pattern. SAXS fits using a spherical core-shell form factor and hard sphere structure factor, as typically done for poloxamer micelles,[40,42–47] indicate that prior to magnetization, P335 micelles have a total radius, R_t of 69.7 ± 0.6 Å, consisting of a largely insoluble PPO core and PEO corona. These micelles coexist in solution with ~32% unimers at 20 °C, determined by differential scanning calorimetry (DSC, **Fig. S26b**). With increasing temperature, the DSC heat flow trace exhibits a single, broad endothermic peak – corresponding to the caloric penalty for removing PPO groups from solution when unimers are added to micelles.[43,48] Thus at 20 °C prior to magnetization, the micelles are small enough and the unimer fraction is large enough that adjacent micelles do not overlap, leading to the low observed complex viscosity, η^*.[49]

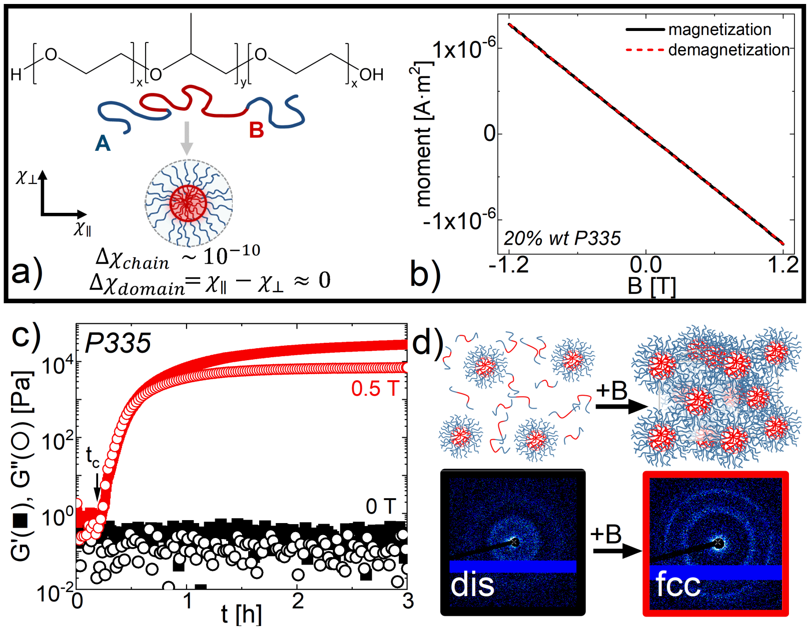

Figure 1: Anomalous phase formation in aqueous 20% wt PEO-PPO-PEO poloxamer 335. a) Poloxamer chemical and spherical micelle structure; the magnetic susceptibility anisotropy $\Delta\chi$ is ~0 based on the difference between PEO (A) and PPO (B) blocks, $\Delta\chi_{chain}$, and the spherical micelle shape, $\Delta\chi_{domain}$. b) P335 magnetic moment vs. $\boldsymbol{B}$ indicates weak diamagnetism. c) Oscillatory magnetorheology of P335 (red, 0.5 T, 20 °C) reveals a rapid increase in G' and G'' following a critical magnetization time t_c, which corresponds to a disordered micelle (*dis*)-to-face centered cubic (*fcc*) ordering transition (d). 1D intensities for the 2D patterns in (d) are in **Fig. 2.**

Oscillatory rheological time sweeps of P335 solutions at 0.5 T detect a transition from a low viscosity liquid ($\eta^* \sim 10^{-2}$ Pa·s) to an ordered soft solid following a critical magnetization time, t_c, of $t_c = 20 \pm 4$ min (**Figs. 1c, S11a**). Following this critical time, the dynamic moduli of 20% P335 rapidly increase with further magnetization (**Fig. 1c**). This large increase in the storage and loss moduli, G' and G'', corresponds to a disorder-to-cubic transition, detected in SAXS via the appearance of Bragg peaks at characteristic q/q^*-positions in the 2D pattern (**Fig. 1d**), where q is the wave vector and q^* is the primary peak wave vector. Frequency sweeps following magnetization demonstrate that the field-induced modulus is enhanced across the frequency spectrum (**Fig. S13**) and that G' is nearly frequency-independent, confirming formation of a solid-like micelle packing. Corresponding controls at zero-field show no increase in modulus over many hours (**Fig. 1c**).

Complementary wide-angle X-ray scattering (WAXS) on magnetized poloxamers confirms that the observed changes in self-assembly and ordering are not due to field-induced crystallization or crystallization-assisted self-assembly (**Section S5**). However interestingly, MR on PEO or PPO homopolymer solutions indicates that both blocks exhibit significant field-induced responses under the appropriate solution conditions – i.e. only when the homopolymer is solubilized (**Fig. S14**) – suggesting that changes in polymer-solvent interactions are critical to observing these effects.[50,51] Notably, $\boldsymbol{B}$-induced responses in both homopolymers are due to field-induced crystallization (**Figs. S14, S15**) and require long magnetization times ($t_{mag} \geq 20$ h). This evidence suggests that while changes in polymer-solvent interactions are crucial to both mechanisms, $\boldsymbol{B}$-induced responses in homopolymers occur via a mechanism distinct from the $\boldsymbol{B}$-induced ordering in poloxamers.

Ordering induced via magnetic fields vs. temperature or concentration change

Moderately concentrated poloxamers undergo thermally-induced DOTs upon increasing temperature, following the addition of unimers into micelles as the PPO midblock becomes increasingly insoluble.[43,44,52] Temperature ramps on 20% P335 solutions at zero-field demonstrate that thermally-induced rheological transition occurs at a temperature of 50 ± 0.4 °C (**Fig. 2a**), ~30 °C higher than the MR temperature, T_{mag}. This significant difference in the thermal vs. magnetic ordering temperatures confirms that the $\boldsymbol{B}$-induced transition at 20 °C is well-separated from the thermally-induced DOT. The zero-field temperature T vs. P335 concentration, ϕ_p, phase diagram compiled from experimental data of ours and others[53,54] (**Fig. 2b**) indicates that in the absence of an applied magnetic field, a DOT can be induced in P335 solutions by increasing the temperature or increasing the P335 content. Corresponding SAXS traces confirm a disorder-to-cubic transition at 0 T by increasing temperature or P335 content, shown at both 55 °C and 40% wt P335 (0 T) in **Fig. 2c**.

Analysis of the lattice parameters, a, obtained by each ordering mechanism indicates that the $\boldsymbol{B}$ field induces ordering via changes to micelle assembly and packing distinct from those obtained when ordering is induced at 0 T by increasing either T or ϕ_p (**Fig. 2c**). Following 3 h of magnetization, P335 micelles arrange into a face-centered cubic (fcc) packing, indicated by Bragg peaks in the 1D SAXS traces at $q/q^* = 1$, $\sqrt{4/3}$, $\sqrt{8/3}$, $\sqrt{11/3}$, 2, and $\sqrt{16/3}$ which correspond to the (111), (200), (220), (311), (222) and (400) crystallographic planes, respectively (red trace, **Fig.**

2c). Here, the P335 micelle radius, R_t, is estimated as half the nearest neighbor distance between micelles on the fcc lattice, yielding R_t = 75.4 ± 0.4 Å (for uncertainty determination, see **Section S9.2**). This large increase in R_t relative to the disordered micelle size before magnetization (69.7 ± 0.6 Å; black trace, **Fig. 2c**) strongly supports the hypothesis that the ***B*** field removes free unimers from solution, adding them to micelles to increase R_t and the micelle aggregation number, N_{agg}.

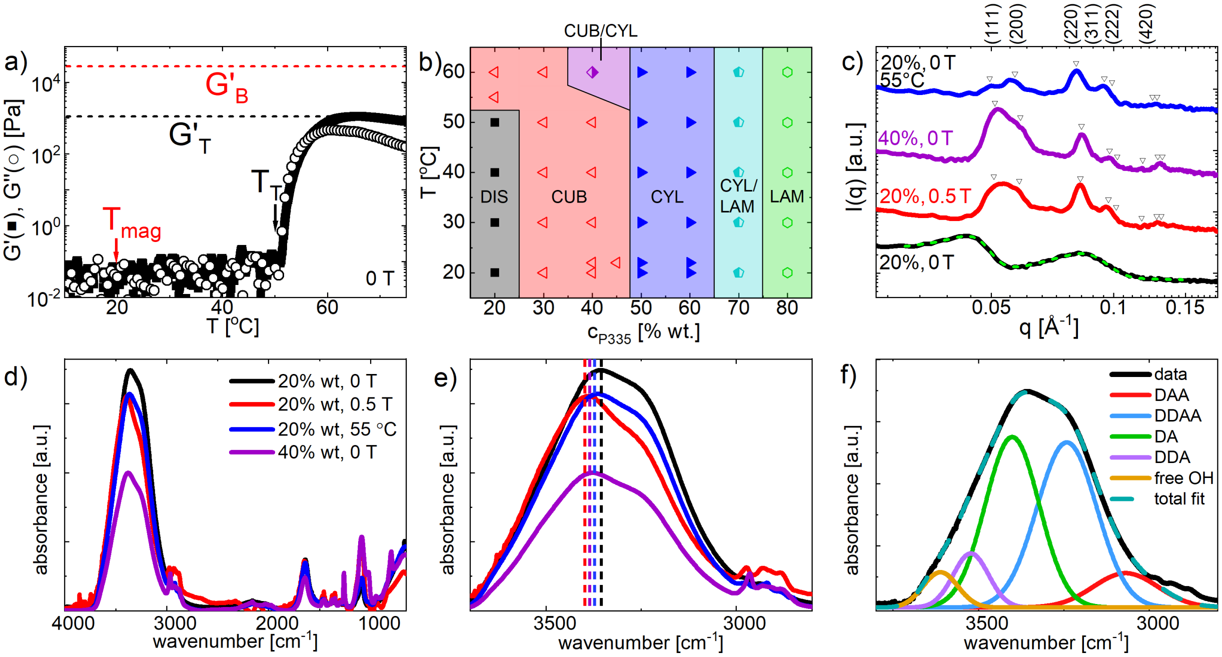

Figure 2: (a) Temperature-dependent rheology for P335 at 0 T indicates a transition near 50 °C, far above T_{MR} (20 °C). The red dashed line shows G'_B, the G' reached at 3 h of magnetization at 0.5T, from Fig 1c. (b) Phase diagram, T vs. P335 % wt at 0 T (**Section S9**, Refs. 53,54). (c) P335 1D SAXS traces, indicating *dis* before (20% wt, black; fit in green) and fcc-packed micelles after 3 h magnetization (0.5 T, red; ▽ indicate crystal planes). The fcc lattice parameter, a, of magnetized micelles is identical to a for a 40% wt control (0 T, purple) and is smaller than a for a T-ordered sample (20% wt, 0 T, 55 °C, blue; **Table S17**). (d) Full wavenumber range and (e) primary water peak (4000–2500 cm^{-1}) FTIR spectra of samples in (c) indicate substantial changes in peak intensity and wavenumber (dotted lines) with ***B***. (f) Representative 5-mode deconvolution fit (dashed blue) of primary water peak data (black) into H-bonding modes; see **Section S7**.

Increasing the temperature of 20% P335 solutions at zero-field above ~50 °C also results in an ordered fcc packing; however, compared to the ***B***-induced transition, the Bragg peaks in the 1D SAXS traces at 55 °C are shifted to lower q-values. This decrease in q^* indicates a larger d-spacing and micelle size, R_t = 77.9 ± 0.3 Å, via thermally-induced ordering relative to ***B***-induced ordering (R_t = 75.4 ± 0.4 Å). This finding suggests that although ***B***-field application increases R_t and N_{agg}, thermally-induced ordering proceeds with fewer micelles of larger R_t and N_{agg} (see **Section S9.7** for calculations and assumptions). The maximum storage modulus obtained due to magnetization, G'_B, is 25-fold greater than that obtained by thermally-induced ordering, G'_T (28 kPa vs. 1.1 kPa, respectively; **Fig. 2a**). The smaller lattice dimension for the $\boldsymbol{B}$-induced transition likely accounts for some of the G' enhancement, as G' for cubic packings scales inversely with microdomain spacing in BCPs.[55] Note that following complete removal of unimers from solution, a significant change in a due to thermal expansion is not anticipated in poloxamers.[41]

Doubling the P335 concentration to 40% wt at zero-field also results in fcc-packed micelles; however remarkably, the lattice dimensions and micelle radius are identical for 20% P335 magnetized at 0.5 T (**Fig. 2c**, red trace) and 40% P335 at 0 T (**Fig. 2c**, purple trace; **Table S14**). Here, R_t = 75.4 ± 0.4 Å – indicating that despite doubling the polymer content, the same number of micelles per volume are in both solutions. This finding strongly suggests that N_{agg} is lower and the interfacial area per chain a_0 increases for the $\boldsymbol{B}$-induced ordered material relative to that formed by increasing P335 content (**Section S9.7**). As R_t and N_{agg} are determined by a balance of core chain stretching vs. a_0 minimization,[43,56,57] this comparison also suggests that the magnetic field significantly alters interactions between P335 and the solvent to facilitate ordering.

Fourier transform infrared spectroscopy (FTIR) on P335 solutions strongly supports that polymer-solvent interactions change due to magnetization (**Fig. 2d, e**), reflected in changes in the stretching and bending modes of water (peaks centered at 3345 and 1640 cm^{-1}) and PEO (2800-3000 and 1000-1530 cm^{-1}). Relative to the disordered, non-magnetized P335 solution (black trace, **Fig. 2d**), FTIR spectra for ordered P335 solutions – magnetized 20% P335 (red), thermally-ordered 20% P335 (blue), and 40% P335 (purple) – all exhibit a decrease in intensity for peaks associated with water at 3345 and 1640 cm^{-1}, consistent with dehydration of the micelle corona upon ordering.[58] While the major water peak of these three solutions shows a significant blue shift as compared to the 20% wt, 0 T control (vertical lines, **Fig. 2e**), the magnetized sample has the largest shift (3363 cm^{-1} to 3387 cm^{-1}). The extent of this blue shift corresponds to corona dehydration,[58–60] further suggesting that $\boldsymbol{B}$ fields more strongly impact polymer-solvent interactions than increasing T.

As corona dehydration is closely connected to water confinement and water bonding,[59] the primary water OH stretching peak at ~3345 cm^{-1} was deconvoluted based on hydrogen bonding modes (**Fig. 2f**), as is commonly done in aqueous systems.[58–62] Here, a sum of Gaussian distributions (commonly between 3 and 6) represents major H-bonding populations, generally distinguished by the number of donor and acceptor electron pairs or coordination number (see **Section S7**). To ensure robustness, both a three and five Gaussian deconvolution were performed (**Section S7.3**); for simplicity, results across methods are discussed based on percentages of three general H-bonding populations. Here, highly-coordinated or "network" water is highly structured but transient, with primarily tetrahedrally-coordinated water molecules breaking and reforming long-range networks.[59] Low-coordinated or "free" water includes small clusters of one to three water molecules with few or no hydrogen bonds.[61] Finally, intermediate-coordinated water exists between these two populations in terms of both number of bonds and cluster size.

Regardless of stimuli – temperature, concentration, or $\boldsymbol{B}$ field – ordered samples contain much less network water and more intermediate water than the disordered control (**Figs. S25, S24; Tables S8, S10**). This result is consistent with prior findings that incorporating unimers into micelles confines water, disrupting large network water clusters thereby increasing intermediate water content.[59] Interestingly, a larger reduction in network water occurs for the $\boldsymbol{B}$-induced vs. T-induced soft solid. High-entropy, low-coordinated water molecules comprise the smallest population for all samples. The low-coordinated water content decreases upon ordering with T or ϕ_p; however surprisingly, $\boldsymbol{B}$-induced ordered soft solids have a similar or higher free water content vs. the disordered control (**Tables S8, S10**). This analysis is consistent with prior findings suggesting that magnetizing water produces smaller, less-coordinated hydrogen bonding clusters.[39,63]

Spherical P333 micelles transform into ordered cylinders in $\boldsymbol{B}$ fields

Comprehensive characterization of the $\boldsymbol{B}$-induced DOT in P335 demonstrated that $\boldsymbol{B}$-fields alter the micelle aggregation number, N_{agg}, and per-chain interfacial area relative to the zero-field T- or ϕ_p-induced DOT, suggesting that this unusual phenomenon is related to $\boldsymbol{B}$-induced changes in polymer-solvent interactions. To examine the universality of this behavior, a second amphiphile, poloxamer 333, was examined (**Fig. 3**). Poloxamer 333 has a PEO weight fraction, w_{PEO}, of ~30% and $M_{n,P333}$ of 5 kDa. P333 has the same PPO midblock molecular weight as P335 and exhibits a similar thermally-induced transition based on zero-field rheology (**Fig. S28**). Importantly, DSC indicates that the caloric penalty for removing the remaining PPO groups from solution above 20 °C is identical in both P333 and P335 (**Section S8**, **Table S11**), i.e., the enthalpy of micellization above 20 °C is identical. Given these similarities, if the field is simply facilitating removal of remaining unimer chains from solution, the transition process and changes in N_{agg} will be similar between these two poloxamers; otherwise, this comparison will unveil more complex behavior.

Similar to P335, P333 displays a distinct $\boldsymbol{B}$-induced DOT after a critical induction time. However for P333, t_c is much longer, 37 ± 5 min (**Fig. 3a, S11b**). SAXS after three hours of magnetization reveals body-centered cubic (*bcc*) packed spherical micelles coexisting with hexagonally-packed cylinders (*cyl*) (**Figs. 3b**), in contrast to the fcc packing observed in P335. The weak *cyl* Bragg peaks after 3 h magnetization become more pronounced with longer t_{mag} (**Fig. S38**).

Remarkably, $\boldsymbol{B}$ field application appears to significantly decrease the P333 micelle radius and N_{agg} upon ordering – in contrast to P335 where both R_t and N_{agg} increase. Here, disordered micelles prior to magnetization have radii of R_t = 70.2 ± 1.0 Å whereas R_t = 66.3 ± 0.5 Å in the *bcc* ordered material (**Tables S12, S18**). Note that the disordered micelle size at 0 T for a higher concentration P333 solution (25% wt, **Tables S12-S13**) is substantially larger than the R_t of the P333 *bcc*-packed micelles under applied $\boldsymbol{B}$-fields – suggesting that $\boldsymbol{B}$-field decreases R_t and N_{agg} relative to increasing polymer concentration. This control also confirms that this $\boldsymbol{B}$-induced change in micelle size is not simply due to experiment artifacts like sample drying.

Similar to P335, the $\boldsymbol{B}$- and T-induced transitions are well-separated (**Fig. 3c**), where T_T~48 °C. Despite that G'_B is nearly four-fold larger in P335 than in P333, the modulus enhancement with magnetization is much greater in P333 – with G'_B nearly 700-fold larger than G'_T (7.7 kPa vs. 11 Pa, respectively). This difference in modulus enhancement is likely due to differences in how the magnetic vs. thermal transitions proceed in P333 vs. P335. Both ordering routes produce an *fcc* packing in 20% wt P335; however, magnetizing 20% wt P333 leads to a *bcc* packing while increasing T leads to formation of disordered rods above ∼35 °C and elongated micelles[49] above ∼48 °C (**Fig. 3c, d**). The weak resulting modulus upon increasing T in 20% wt P333 leads to greater modulus enhancement, as cubic phases are associated with higher moduli than rod or *cyl* phases.[55,64,65] Rod formation is also observed in 25% and 30% wt P333 at high temperatures (**Section S9.8**). As such, magnetizing 20% wt P333 produces ordered phases of spherical micelles completely inaccessible via thermal routes (**Fig. S29-S31**).

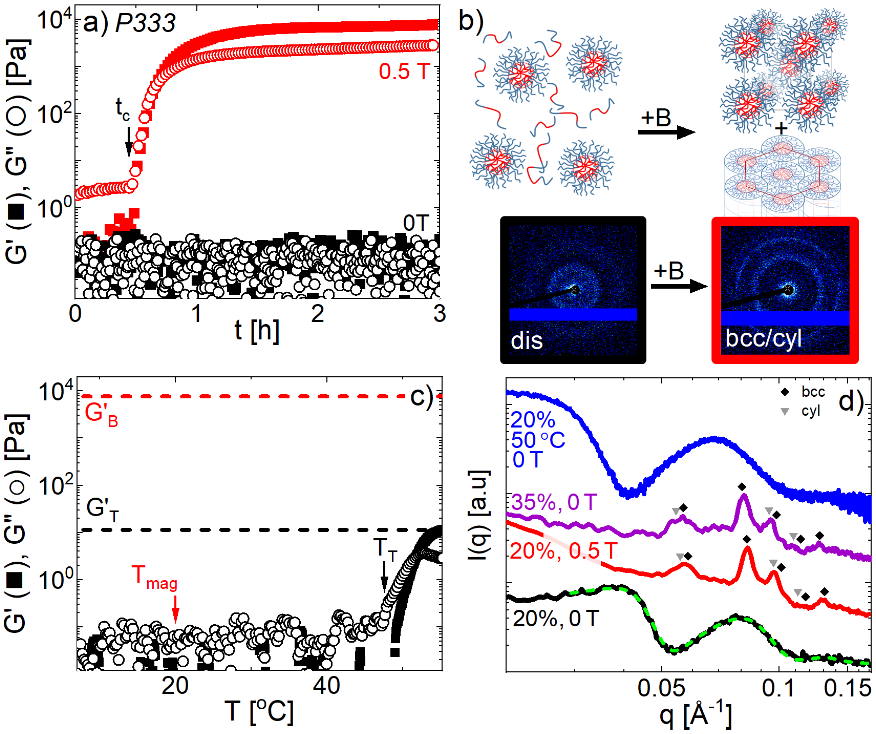

Figure 3: $\boldsymbol{B}$-induced ordering in 20% wt P333. (a) Oscillatory MR (red, 0.5 T, 20 °C) shows that G' and G'' rapidly increase after t_c, corresponding to a DOT. (b) SAXS following 3 h magnetization reveals *bcc* / *cyl* phase coexistence. (c) T-dependent rheology (0 T) indicates a transition near $T_T = 48$ °C, far above T_{mag}; the sample becomes unstable above 55 °C. d) 1D SAXS intensities, indicating *dis* before (20% wt, 0 T, black; fit in green) and *bcc* / *cyl* phase coexistence after 3 h magnetization (red; ◆ ▼ indicate crystal planes). Relative intensities of *bcc* and *cyl* Bragg peaks for 20% wt magnetized P333 are similar to those of a 35% wt control (0 T, purple); *dis* cylindrical micelles are observed with increasing T (20% wt, 0 T, 50 °C, blue); see **Table S13**.

As in P335, magnetized P333 exhibits the same phase behavior as higher concentration, zero-field controls (**Fig. 3d, Table S13**). At zero-field, 35% wt and 40% wt P333 form coexisting *bcc* / *cyl*, whereas a *bcc* packing is observed at 30% wt. The relative intensities of the *bcc* and *cyl* Bragg peaks for magnetized P333 are similar to those for zero-field 35% wt P333 (**Fig. 3d**). Remarkably, the inter-cylinder spacing is smaller in magnetized 20% wt P333 (a=130 Å) vs. in 0 T controls at 35% and 40% wt P333 (~134 Å, **Table S13**). As mass conservation requires 20% wt cylinders to exhibit a greater per-chain interfacial area (**Section S9.7**), low-intensity ***B*** fields afford access to *cyl* packings inaccessible by increasing ϕ_p.

Further magnetization leads to order-to-order transitions (OOTs)

The coexisting *bcc* and *cyl* phases in P333 after three hours of magnetization suggest that ***B***-induced ordering may proceed by a multi-step mechanism, which may result from changing solvent quality under applied field. We hypothesize this multi-step mechanism follows a path across the T vs. ϕ_p phase diagram at zero-field (**Figs. 2b, S28**), similar to the previously described 'trajectory approach',[66,67] where ***B***-field may cause effects similar to increasing T (vertical trajectory on phase diagram) or increasing ϕ_p (horizontal trajectory). To validate this multiple-step transition, P333 and P335 were magnetized for various times to map the phase transition pathways (**Fig. 4**).

P335 forms an fcc packing after three hours of magnetization (**Figs. 4a, b**), and similar fcc packings result when P335 is magnetized for nearly four more hours (**Fig. S36**). Here, d-spacings of the fcc phases formed after five magnetization times are remarkably consistent (R_t = 75.5 ± 0.4 Å, **Table S17**). Interestingly, slightly longer magnetization times of nearly 7 h lead to clearly coexisting fcc and *cyl* phases (**Figs. 4b, S37**). This phase coexistence does not persist, however, as *cyl* phases with little to no cubic phase coexistence are observed for magnetization times between 7.5 h and 12 h (**Figs. 4b, S36**). The d-spacings for *cyl* phases formed at different magnetization times are remarkably similar (**Table S17**). This comprehensive dataset strongly suggests that P335 indeed follows a multi-step trajectory in which disordered micelles transform into fcc packings followed by a cubic-to-cylinder transition, over the course of 12 h of magnetization at 0.5 T. This multi-step transition is similar to the sequence observed with increasing ϕ_p (horizontal trajectory) on the 0 T phase diagram (**Fig. 2b**), where fcc packings are observed up until ~45% wt P335, and *cyl* phases emerge at ~50% wt P335. A similar $fcc \rightarrow cyl$ transition has also been observed upon temperature elevation in another 50% wt PEO poloxamer known as P235.[68]

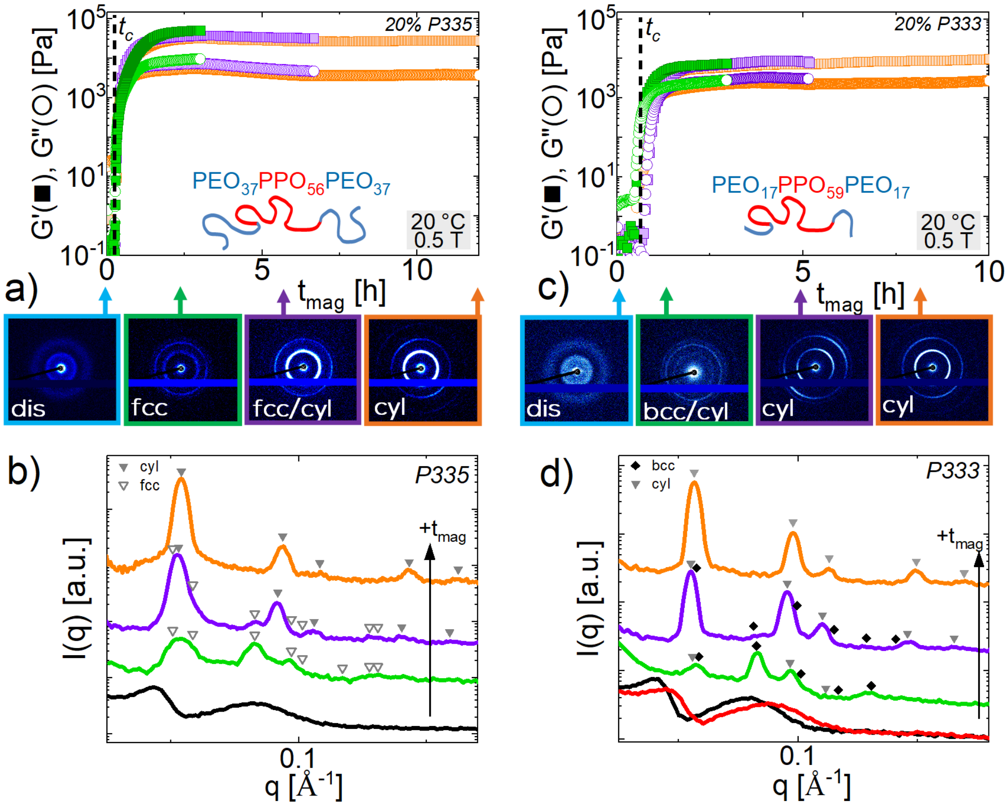

Figure 4: Ordering transition pathways in P335 (a,b) and P333 (c,d). (a,c) Repeated MR yields highly reproducible t_c and field-induced moduli, G'_B. Corresponding 2D SAXS patterns (a,c) and 1D intensities (b,d) for increasing t_{mag} reveal a *dis* → *fcc* → *cyl* transition for P335 (a,b) and a *dis* → *bcc* → *cyl* transition for P333 (c,d). (d) After 2 h magnetization, the P333 induced phase rapidly relaxes (red); however, a dramatically smaller disordered micelle size, similar to R_t observed in the *bcc* lattice at longer t_{mag}, persists – seen by the shift in both broad peaks to higher q-values.

This trajectory-like behavior is not unique to P335, as a similar multi-step transition is observed in supplementary experiments on P407, which instead undergoes a *dis*-to-*fcc* transition, followed by a *fcc*-to-*bcc* transition (**Section S6**). Interestingly, the number of micelles per volume, n/V, is not preserved during this *fcc*-to-*bcc* transition transition, changing ∼20% (**Section S6**). This increase in micelle number density in the *bcc* phase with further magnetization implies that the $\boldsymbol{B}$ field makes the formation of smaller, lower N_{agg} micelles more thermodynamically favorable – consistent with results from P335 and P333. These experiments also demonstrate that the induced structure and increase in n/V are reversible after field removal, as P407 eventually relaxes from a *bcc* packing back to the *fcc* packing of lower n/V.

Paired with the zero-field *bcc*-to-*cyl* transition observed with increasing P333 content, the *bcc* / *cyl* coexistence in P333 magnetized for 3 h suggests that this poloxamer undergoes a *dis* → *bcc* → *cyl* transition over fairly short magnetization times (**Fig. 4c, d**). After 5 h magnetization, *cyl* Bragg peaks become more prominent, although a clear *bcc* coexistence is observed. However, after 8 h magnetization, the *bcc* peaks largely vanish while the *cyl* peaks increase in intensity relative to the 5 h magnetization; a similar structure is observed after 10 h magnetization (**Figs. S38-S39**). As in magnetized P335, the *cyl* and cubic d-spacings are remarkably consistent across magnetization times; only the relative prominence of one phase vs. another changes appreciably with increasing t_{mag}. Interestingly, while the critical time is nearly double that for P333 vs. P335, the cubic → *cyl* transition occurs over more rapid timescales than in P335. One explanation is that this more rapid OOT timescale reflects that *cyl* formation is more thermodynamically favorable in the lower PEO content P333,[49] reflected by the *cubic* → *cyl* transition at lower ϕ_p on the 0 T phase diagram for P333 vs. P335 (**Fig. 2b** vs. **Fig. S28**).

Unlike in P335, no fcc packings are observed for P333 at shorter magnetization times or in the 0 T SAXS. At zero-field, P333 and P335 micelles have nearly identical interfacial areas per chain (**Table S16**), yet each P333 chain has substantially less PEO -- thus *bcc* formation here likely reflects that the shorter PEO blocks in P333 form micelles with less dense coronas.[69] A direct *dis*-to-*bcc* transition in P333 is supported by magnetization experiments at two hours (**Fig. 4d**, red trace). At these short times, P333 forms a soft solid in the rheometer but the sample relaxes into disordered micelles by the time the SAXS is performed. However, consistent with the smaller *bcc*-packed micelles observed after 3 h magnetization, the smaller micelle size persists upon relaxation – seen by the clear shift of the two broad scattering peaks to higher q-values. Here, a reduction in the disordered R_t of 7.2 ± 1.2 Å is observed vs. R_t prior to magnetization (**Table S12**). This magnetized micelle radius is also significantly smaller than the disordered R_t observed at higher concentrations at 0 T (**Fig. S34**, **Table S12**), again confirming that field-induced changes in micelle size and ordering are distinct from those observed with increasing T or ϕ_p at zero-field. Finally, the remarkable consistency of the fcc, *bcc*, and *cyl* lattice parameters across t_{mag} for both P333 and P335 suggests that while $\boldsymbol{B}$-field alters micelle hydration, the preferred packing dimensions for a given ordered phase remain the same. This finding also suggests that artifacts like gradual drying of the sample are not realistic explanations of the observed phase behavior.

Discussion

To our knowledge, the disorder-to-cubic transitions here are the first observations of magnetic field-induced ordering of diamagnetic spheres. We are similarly unaware of any work demonstrating a stable field-induced sphere-to-rod transition at low field intensities, although at high field intensities, electric and magnetic fields can elongate spherical micelles into ellipsoids.[70] Furthermore, this work is the first to demonstrate a direct magnetically-induced OOT in an entirely diamagnetic BCP system – without requiring addition of magnetite nanoparticles or magneto-thermal annealing.[27] Below, we briefly review plausible explanations for this behavior, and then propose a most likely mechanism of $\boldsymbol{B}$-induced ordering in these materials.

To date, $\boldsymbol{B}$-responsiveness in diamagnetic BCPs has typically resulted from alignment of anisotropic species or domains, driven by a high $\Delta\chi$ mesogen or a high $\Delta\chi$ between blocks.[16,28,71–73] However here, the micelles are spherical ($\Delta\chi_{phase} \sim 0$) and the magnetic susceptibility anisotropy based on the PEO and PPO blocks is also nearly zero ($\Delta\chi_{chain} \sim 10^{-10}$). Alignment during crystallization occurs due to geometric anisotropy of the growing crystal, enhancing $\Delta\chi$.[37,74] In PEO-based BCPs with large LC mesogens, PEO crystallization is typically suppressed or confined and does not drive alignment;[71,72,75] however, PEO crystallization can drive orientation in BCPs without LC mesogens.[37] Indeed here – over timescales that are one to two orders of magnitude longer than the poloxamer $\boldsymbol{B}$-induced ordering – PEO and PPO homopolymers can exhibit $\boldsymbol{B}$-induced crystallization (**Section S5**). Yet, WAXS and FTIR on poloxamers do not show any crystallization peaks, ruling out $\boldsymbol{B}$-induced crystallization or crystallization-assisted self-assembly.[15,31] However, changes in polymer chain conformation similar to those during crystallization could plausibly explain some of the observed changes in packing, especially when OOTs occur after long t_{mag}.

Other alternative explanations include the presence of impurities, concentration gradients or macroscopic phase separation, sample drying, or other artifacts. However, chemical analysis confirms that the samples are free of ferro- or paramagnetic impurities, and magnetic analysis confirms the expected diamagnetic behavior (**Section S3.1**). Poloxamer samples are clear and appear homogeneous following long t_{mag}, suggesting an absence of macrophase separation and concentration gradients (**Fig. S6**). Magnetized poloxamers relax back to the same structure as non-magnetized controls (**Section S6**), confirming that the sample is not irreversibly altered. The smaller structure sizes observed with magnetization are also not observed at higher ϕ_p, as would be expected if this phenomenon were due to drying. This response is also robust to polymer batch, salt, and diblock impurities (**Section S3.2**). Finally, samples placed on permanent magnets display similar behaviors, verifying that this response is not dependent on the magnetorheometer.

We instead propose that, due to the presence of solvent, these changes in phase behavior are a consequence of molecular-level processes, namely alterations to solvent quality and polymer-solvent interactions that dictate self-assembly energetics. Our results suggest that $\boldsymbol{B}$ fields alter solvent quality by reducing or weakening polymer-solvent interactions and strengthening interchain interactions, in agreement with Vshikov and others.[39,62,76] Numerous studies have shown that $\boldsymbol{B}$ fields significantly impact the thermodynamic, optical, electrical, and surface properties of water.[77–79] While the influence of $\boldsymbol{B}$ fields on hydrogen bonding in water has been contested,[80–84] a competitive proposed mechanism unifies these theories. Here $\boldsymbol{B}$ fields break intra-cluster hydrogen bonds but strengthen inter-cluster bonds, resulting in smaller water clusters.[63] These changes in water structure and polarity may account for some of the changes in water bonding modes observed in the P335 FTIR spectra, especially the increase in free and multimer water with $\boldsymbol{B}$.

The proposed changes in solvation are consistent with the observed $\boldsymbol{B}$-induced ordering in both P333 and P335. These DOTs suggest that unimers in solution prior to magnetization are added to micelles enabling a soft solid to form – implying that the $\boldsymbol{B}$ field facilitates unimer removal from solution. This process is at least in part similar to the effect of increasing T, which worsens solvent quality and similarly facilitates unimer removal via an endothermic process. Thus, even if poloxamer chains were to eventually crystallize, given the multiple-hour timescale associated with homopolymer $\boldsymbol{B}$-induced crystallization, any potential PEO or PPO crystals would seemingly play little role in the transition onset.

Notably, in poloxamers like P333 at 20% wt, magnetization creates significantly smaller micelles relative to the disordered micelles prior to magnetization (20% wt) and at 0 T at higher P333 content (25% wt). These zero-field controls help eliminate sample drying as a potential explanation for this anomalous behavior, as the resulting microstructure upon drying would be expected to mirror that of higher ϕ_p P333 solutions. Further, the reduced R_t with magnetization is observed in both the *bcc* ordered material and following relaxation after short t_{mag}. At 20% wt P333 and 0 T, increasing T does not yield cubic phases and instead leads to rod formation – suggesting that the volume fraction of P333 spherical micelles may be insufficient to form a system-spanning cubic packing. Accordingly, $\boldsymbol{B}$-induced ordering likely only occurs because magnetization reduces the P333 micelle size significantly, thereby increasing the overall micelle volume fraction and enabling a system-spanning cubic packing to form.

Why does P333 have a critical time twice that of P335, despite these two solutions having identical micellization enthalpies above 20 °C? If unimer removal from solution and insertion into micelles was the only process that $\boldsymbol{B}$ field impacted, the two DOTs would appear similar. However, the magnetized P335 R_t is larger than R_t before magnetization (20% wt, 0 T). While the magnetized R_t and N_{agg} are slightly smaller than that observed at zero-field with increasing T, a significant number of the unimers in solution can be added to existing P335 micelles upon magnetization, leading to the observed >6 Å increase in R_t with magnetization. As such, only a small fraction of additional micelles (relative to increasing T) must be created by applying $\boldsymbol{B}$-field for P335 to form a cubic packing. Conversely, R_t for P333 upon magnetization significantly decreases relative to its zero-field disordered R_t. Here, the micelle volume decreases by over 25% upon magnetization. Thus, one potential explanation for the longer t_c in P333 is that beyond the time required to remove unimers from solution, the additional time required for mass rearrangement – i.e. removing chains from existing micelles and forming new micelles – lengthens t_c relative to t_c for P335.

What accounts for these differences in how R_t and N_{agg} change upon magnetization for P333 vs. P335? SANS indicates that while P333 and P335 at 20% wt (0 T) have similar R_t, the N_{agg} for P333 micelles is >40% greater (**Sections S9.5,S9.6**). Here, the micelle core is much larger for

P333 whereas the coronas are larger in P335 due to the bulky PEO end blocks. Thus the starting conditions, i.e. the micelles present when $\boldsymbol{B}$-field is applied, are substantially different. The higher initial N_{agg} for P333 micelles means that the PPO core blocks are significantly more stretched, incurring an entropic penalty. Micelle shape changes like elongation are favored over an increase in the spherical micelle R_t when the entropic penalty for core chain stretching exceeds the benefit of further reducing PPO-solvent contact via unimer addition, often when the core size equals the length of the stretched PPO chain.[49,56,57] Thus, simply adding all unimers to existing, already-large P333 micelles would likely incur a sphere-to-rod transition, as occurs with increasing T at 0 T.

Conversely, chains in P335 micelles prior to magnetization are substantially less stretched despite equivalent R_t, as N_{agg} is much smaller. Accordingly, existing micelles can accommodate addition of numerous unimers upon magnetization before becoming fully stretched – enabling a system-spanning cubic packing to form primarily by forming larger micelles, rather than more micelles. The ordering behavior of 20% wt P335 at 0 T also shows that increasing T is sufficient to form a cubic packing, suggesting that P335 micelles at 20 °C are at a high enough volume fraction that inserting remaining unimers primarily into existing micelles is sufficient to induce ordering – which is not the case for P333. Notably, the P335 micelle volume fraction at 20 °C is ~15% larger than that for P333 (**Section S9.6**). The precise reason that P333 micelles become smaller instead of undergoing a sphere-to-rod transition while P335 micelles instead increase in size is unclear. However, one reasonable explanation is that adding a unimer to a micelle in which the core chains are already tightly packed and highly stretched is more difficult than adding a unimer to a micelle with a lower packing density. Additionally, the most favorable chain packing for either system does appear to be altered by the presence of $\boldsymbol{B}$-field, as the interfacial area per chain in the ordered phase increases vs. the micelles formed with increasing T or ϕ_p in both cases. One possible cause of this increase in a_0 is that the $\boldsymbol{B}$-field induces additional associations between PEO and water in the outer micelle corona, leading each PEO end block to assume a greater effective volume. Association of water with free PEO has been shown to promote micellization in poloxamers due to a reduction in available water content,[40,85,86] which could also help facilitate ordering.

Finally, in both poloxamers, any changes in solvent quality and chain conformation during magnetization result in a cubic-to-*cyl* OOT. However, despite the much longer t_c, the cubic-to-*cyl* OOT happens more rapidly in P333 than P335. This more rapid OOT in P333 thus may reflect its smaller cubic phase window on the zero-field T vs. ϕ_p phase diagram. As shown previously,[49,87,88] P333 easily forms rods and wormlike structures due to its relatively small PEO fraction, whereas the large PEO end groups in P335 hinder formation of elongated structures. Unsurprisingly, P333 at zero-field forms rods or cylinders at substantially lower T or ϕ_p than P335 (**Section S9**).[43,49,88]

Conclusion

The anomalous disorder-to-order transition (DOT) induced in diamagnetic poloxamers by low-intensity magnetic fields provides a unique route for developing well-ordered BCP materials. Unlike in all previous examples of ordered polymeric materials in magnetic fields, this system does not respond to magnetic fields via domain alignment. As such, we have shown the first example of isotropic BCP building blocks ordering into a nonaligned, i.e. cubic, ordered phase in response to magnetic fields. This approach is particularly promising for advanced materials development, as the proposed solvation mechanism is not specific to BCP chemistry.

Via magnetorheology, X-ray scattering, differential scanning calorimetry and vibrational spectroscopy, the magnetic field-induced DOT is shown to be related to magnetic field-altered polymer-solvent interactions – not due to field-induced crystallization, as is observed in homopolymer solutions. The precise molecular mechanisms leading to these field-altered polymer-solvent interactions will be the subject of immediate future work. The particular ordered phase that forms due to magnetic field processing depends on both the amphiphile characteristics and magnetization time. For both P333 and P335, the phase trajectory as a function of magnetization time generally follows the zero-field phase diagram with increasing polymer content – cubic packings of spherical micelles followed by hexagonal packings of cylindrical micelles. However, the interfacial area per poloxamer chain greatly increases for magnetized micelles and cylinders vs. those formed by increasing the concentration.

Promisingly, materials processed via magnetic fields exhibit significant mechanical and structural improvements over those materials processed via thermal methods. The dynamic moduli of these aqueous BCP solutions begin increasing rapidly in less than one hour of magnetization for both P333 and P335. As a result of these field-induced transitions, G' and G'' increase by four orders of magnitude, demonstrating a modulus enhancement two to four orders of magnitude greater than that observed by thermally-induced ordering. P333 shows a morphology distinct from that of thermal processing (disordered rods) when instead exposed to magnetic fields (*bcc*). Interestingly, while magnetically-ordered P335 has significantly higher moduli, both T- and $\boldsymbol{B}$-ordered samples have the same fcc packing and a similar lattice parameter, suggesting that minor changes in a only partially account for the significant modulus enhancement. Accordingly, this new approach to ordering BCPs affords access to structures and d-spacings inaccessible by changing temperature or polymer concentration. As a result, magnetizing aqueous BCPs in this manner offers an innovative platform for developing BCP materials with precisely-tuned properties.

Acknowledgement

This material is based upon work supported by the National Science Foundation under Grant No. DMR-2143162. Researchers contributing to this work were additionally supported by the National Science Foundation (NSF) Graduate Research Fellowship under Award 2237827 (G.V.K.). Any opinions, findings, and conclusions or recommendations expressed in this material are those of the author(s) and do not necessarily reflect the views of the National Science Foundation. SAXS data were acquired in the Characterization Facility at the University of Minnesota (UMN), which receives partial support from NSF through the MRSEC program (DMR-2011401). Synchrotron SAXS experiments were conducted at the Advanced Photon Source (APS), Sector 5 DuPont-Northwestern-DOW Collaborative Access Team (DND-CAT). DND-CAT is supported by E.I. DuPont de Nemours & Co., the Dow Chemical Company and Northwestern University. SANS experiments were conducted at the NG-7 30 m SANS instrument at the Center for Neutron Research (NCNR), National Institute of Standards and Technology (NIST), Gaithersburg, MD. We thank the Anton Paar VIP Program and acknowledge the Institute for Rock Magnetism at UMN and Dr. Dario Bilardello for providing the SQUID and VSM facilities. The authors thank Karthika

Suresh for performing preliminary MR experiments, and Timothy Lodge for useful discussions and suggestions.

Supporting Information Available

Supporting Information contains: Additional materials and methods; Supplementary characterization data and calculations (zero-field and after MR): small angle X-ray and neutron scattering (SAXS/SANS), oscillatory rheology, differential scanning calorimetry (DSC), Fourier transform infrared spectroscopy (FTIR), nuclear magnetic resonance (NMR), size exclusion chromatography (SEC), magnetic moment characterization, etc.; Supplementary MR and SAXS experiments on P407; Wide angle X-ray scattering on poloxamers and homopolymers.

References

(1) Attard, G. S.; Bartlett, P. N.; Coleman, N. R. B.; Elliott, J. M.; Owen, J. R.; Wang, J. H. Mesoporous platinum films from lyotropic liquid crystalline phases. *Science* **1997**, *278*, 838–840.

(2) Chen, A.; Komura, M.; Kamata, K.; Iyoda, T. Highly ordered arrays of mesoporous silica nanorods with tunable aspect ratios from block copolymer thin films. *Adv. Mater.* **2008**, *20*, 763–767.

(3) Drummond, C. J.; Fong, C. Surfactant self-assembly objects as novel drug delivery vehicles. *Curr. Opin. Colloid Interface Sci.* **1999**, *4*, 449–456.

(4) Young, W. S.; Epps III, T. H. Salt doping in PEO-containing block copolymers: counterion and concentration effects. *Macromolecules* **2009**, *42*, 2672–2678.

(5) Yamamoto, T.; Kimura, T.; Komura, M.; Suzuki, Y.; Iyoda, T.; Asaoka, S.; Nakanishi, H. Block Copolymer Permeable Membrane with Visualized High- Density Straight Channels of Poly (ethylene oxide). *Adv. Funct. Mater.* **2011**, *21*, 918–926.

(6) Glass, R.; Moller, M.; Spatz, J. P. Block copolymer micelle nanolithography. *Nanotechnology* **2003**, *14*, 1153.

(7) Bita, I.; Yang, J. K. W.; Jung, Y. S.; Ross, C. A.; Thomas, E. L.; Berggren, K. K. Graphoepitaxy of self-assembled block copolymers on two-dimensional periodic patterned templates. *Science* **2008**, *321*, 939–943.

(8) Park, S.; Lee, D. H.; Xu, J.; Kim, B.; Hong, S. W.; Jeong, U.; Xu, T.; Russell, T. P. Macroscopic 10-terabit-per-square-inch arrays from block copolymers with lateral order. *Science* **2009**, *323*, 1030–1033.

(9) Yavitt, B. M.; Fei, H.; Kopanati, G.; Li, R.; Fukuto, M.; Winter, H. H.; Watkins, J. J. Long-Range Lamellar Alignment in Diblock Bottlebrush Copolymers via Controlled Oscillatory Shear. *Macromolecules* **2020**, *53*, 2834–2840.

(10) Powers, L.; Clark, N. A. Preparation of large monodomain phospholipid bilayer smectic liquid crystals. *Proc. Natl. Acad. Sci. U.S.A.* **1975**, *72*, 840–843.

(11) Ruppel, M.; Pester, C. W.; Langner, K. M.; Sevink, G. J. A.; Schoberth, H. G.; Schmidt, K.; Urban, V. S.; Mays, J. W.; BoÌ^ker, A. Electric field induced selective disordering in lamellar block copolymers. *ACS Nano* **2013**, *7*, 3854–3867.

(12) Pester, C. W.; Liedel, C.; Ruppel, M.; Boker, A. Block copolymers in electric fields. *Prog. Polym. Sci.* **2017**, *64*, 182–214.

(13) McCulloch, B.; Portale, G.; Bras, W.; Segalman, R. A. Increased Order–Disorder Transition Temperature for a Rod-Coil Block Copolymer in the Presence of a Magnetic Field. *Macromolecules* **2011**, *44*, 7503–7507.

(14) Tao, Y.; Zohar, H.; Olsen, B. D.; Segalman, R. A. Hierarchical Nanostructure Control in Rod-Coil Block Copolymers with Magnetic Fields. *Nano Lett.* **2007**, *7*, 2742–2746.

(15) Ebert, F.; Thurn-Albrecht, T. Controlling the orientation of semicrystalline polymers by crystallization in magnetic fields. *Macromolecules* **2003**, *36*, 8685–8694.

(16) Gopinadhan, M.; Choo, Y.; Kawabata, K.; Kaufman, G.; Feng, X.; Di, X.; Rokhlenko, Y.; Mahajan, L. H.; Ndaya, D.; Kasi, R. M.; Osuji, C. O. Controlling orientational order in block copolymers using low-intensity magnetic fields. *Proc. Natl. Acad. Sci.* **2017**, *114*, E9437–E9444.

(17) Majewski, P. W.; Yager, K. G. Rapid ordering of block copolymer thin films. *J. Phys. Condens. Matter* **2016**, *28*, 403002.

(18) Xu, T.; Zhu, Y.; Gido, S. P.; Russell, T. P. Electric field alignment of symmetric diblock copolymer thin films. *Macromolecules* **2004**, *37*, 2625–2629.

(19) Mansky, P.; DeRouchey, J.; Russell, T.; Mays, J.; Pitsikalis, M.; Morkved, T.; Jaeger, H. Large-area domain alignment in block copolymer thin films using electric fields. *Macromolecules* **1998**, *31*, 4399–4401.

(20) Morkved, T.; Lu, M.; Urbas, A.; Ehrichs, E.; Jaeger, H.; Mansky, P.; Russell, T. Local control of microdomain orientation in diblock copolymer thin films with electric fields. *Science* **1996**, *273*, 931–933.

(21) Schmidt, K.; Schoberth, H. G.; Ruppel, M.; Zettl, H.; Hänsel, H.; Weiss, T. M.; Urban, V.; Krausch, G.; Böker, A. Reversible tuning of a block-copolymer nanostructure via electric fields. *Nat. Mater.* **2008**, *7*, 142–145.

(22) Gibertini, M.; Koperski, M.; Morpurgo, A.; Novoselov, K. Magnetic 2D materials and heterostructures. *Nature Nanotech.* **2019**, *14*, 408–419.

(23) Streubel, R.; Fischer, P.; Kronast, F.; Kravchuk, V. P.; Sheka, D. D.; Gaididei, Y.; Schmidt, O. G.; Makarov, D. Magnetism in curved geometries. *J. Phys. D. Appl. Phys.* **2016**, *49*, 363001.

(24) Feng, X.; Kawabata, K.; Cowan, M. G.; Dwulet, G. E.; Toth, K.; Sixdenier, L.; Haji-Akbari, A.; Noble, R. D.; Elimelech, M.; Gin, D. L. Single crystal texture by directed molecular self-assembly along dual axes. *Nat. Mater.* **2019**, *18*, 1235–1243.

(25) Majewski, P. W.; Osuji, C. O. Controlled alignment of lamellar lyotropic mesophases by rotation in a magnetic field. *Langmuir* **2010**, *26*, 8737–8742.

(26) Tolbert, S. H.; Firouzi, A.; Stucky, G. D.; Chmelka, B. F. Magnetic field alignment of ordered silicate-surfactant composites and mesoporous silica. *Science* **1997**, *278*, 264–268.

(27) Ren, B. H.; Chu, C. Y.; Jhang, B. S. Magnetic Field-Induced Order–Order Transition from Hexagonally Packed Cylinders to Lamellae with Large-Scale Orientations in a Block Copolymer/Magnetic Nanoparticle Nanocomposite Film. *Macromolecules* **2023**, *56*, 3363–3373.

(28) Rokhlenko, Y.; Gopinadhan, M.; Osuji, C. O.; Zhang, K.; O'Hern, C. S.; Larson, S. R.; Gopalan, P.; Majewski, P. W.; Yager, K. G. Magnetic alignment of block copolymer microdomains by intrinsic chain anisotropy. *Phys. Rev. Lett.* **2015**, *115*, 258302.

(29) Gopinadhan, M.; Choo, Y.; Mahajan, L. H.; Ndaya, D.; Kaufman, G.; Rokhlenko, Y.; Kasi, R. M.; Osuji, C. O. Directing block copolymer self-assembly with permanent magnets: photopatterning microdomain alignment and generating oriented nanopores. *Mol. Sys. Des. Eng.* **2017**, *2*, 549–559.

(30) Larson, R. G. *The structure and rheology of complex fluids*; Oxford University Press New York, 1999; Vol. 150.

(31) Kimura, T. Study on the effect of magnetic fields on polymeric materials and its application. *Polymer J.* **2003**, *35*, 823.

(32) Garrido, L. Magnetic orientation of diamagnetic amorphous polymers. *J. Polym. Sci. Pol. Phys.* **2010**, *48*, 1009–1015.

(33) Majewski, P. W.; Gopinadhan, M.; Osuji, C. O. Magnetic field alignment of block copolymers and polymer nanocomposites: Scalable microstructure control in functional soft materials. *J. Polym. Sci. Pol. Phys.* **2012**, *50*, 2–8.

(34) Firouzi, A.; Schaefer, D. J.; Tolbert, S. H.; Stucky, G. D.; Chmelka, B. F. Magnetic-Field-Induced Orientational Ordering of Alkaline Lyotropic Silicate-Surfactant Liquid Crystals. *J. Am. Chem. Soc.* **1997**, *119*, 9466–9477.

(35) Löwik, D.; Shklyarevskiy, I. O.; Ruizendaal, L.; Christianen, P.; Maan, J. C.; van Hest, J. A

Highly Ordered Material from Magnetically Aligned Peptide Amphiphile Nanofiber Assemblies. *Adv. Mater.* **2007**, *19*, 1191–1195.

(36) Rokhlenko, Y.; Moschovas, D.; Miskaki, C.; Chan, E. P.; Avgeropoulos, A.; Osuji, C. O. Creating Aligned Nanopores by Magnetic Field Processing of Block Copolymer/Homopolymer Blends. *ACS Macro Lett.* **2019**, *8*, 261–266.

(37) Grigorova, T.; Pispas, S.; Hadjichristidis, N.; Thurn-Albrecht, T. Magnetic field induced orientation in diblock copolymers with one crystallizable block. *Macromolecules* **2005**, *38*, 7430–7433.

(38) Rokhlenko, Y.; Majewski, P. W.; Larson, S. R.; Gopalan, P.; Yager, K. G.; Osuji, C. O. Implications of Grain Size Variation in Magnetic Field Alignment of Block Copolymer Blends. *ACS Macro Lett.* **2017**, *6*, 404–409.

(39) Neal, C. A.; Shetty, A. M.; Linn, J. D.; Quan, M. C.; Casas, J. D.; Calabrese, M. A. Magnetic field-dependent rheological behavior of thermoresponsive poly (N-isopropylacrylamide) solutions. *Rheol. Acta* **2024**, *63*, 493–512.

(40) White, J. M.; Calabrese, M. A. Impact of small molecule and reverse poloxamer addition on the micellization and gelation mechanisms of poloxamer hydrogels. *Coll. Surf. A Physicochem. Eng. Asp.* **2022**, *638*, 128246.

(41) White, J. M.; Garza, A.; Griebler, J. J.; Bates, F. S.; Calabrese, M. A. Engineering the Structure and Rheological Properties of P407 Hydrogels via Reverse Poloxamer Addition. *Langmuir* **2023**, *39*, 5084–5094.

(42) Wanka, G.; Hoffmann, H.; Ulbricht, W. The aggregation behavior of poly-(oxyethylene)-poly-(oxypropylene)-poly-(oxyethylene)-block-copolymers in aqueous solution. *Colloid Polym. Sci.* **1990**, *268*, 101–117.

(43) Wanka, G.; Hoffmann, H.; Ulbricht, W. Phase Diagrams and Aggregation Behavior of Poly(oxyethylene)-Poly(oxypropylene)-Poly(oxyethylene) Triblock Copolymers in Aqueous Solutions. *Macromolecules* **1994**, *27*, 4145–4159.

(44) Mortensen, K.; Brown, W. Poly (ethylene oxide)-poly (propylene oxide)-poly (ethylene oxide) triblock copolymers in aqueous solution. The influence of relative block size. *Macromolecules* **1993**, *26*, 4128–4135.

(45) Alexandridis, P.; Hatton, T. A. Poly (ethylene oxide) poly (propylene oxide) poly (ethylene oxide) block copolymer surfactants in aqueous solutions and at interfaces: thermodynamics, structure, dynamics, and modeling. *Coll. Surf. A Physicochem. Eng. Asp.* **1995**, *96*, 1–46.

(46) Yang, L.; Alexandridis, P.; Steytler, D. C.; Kositza, M. J.; Holzwarth, J. F. Small-Angle Neutron Scattering Investigation of the Temperature-Dependent Aggregation Behavior of the Block Copolymer Pluronic L64 in Aqueous Solution. *Langmuir* **2000**, *16*, 8555–8561.

(47) Pedersen, J. S.; Gerstenberg, M. C. The structure of P85 Pluronic block copolymer micelles determined by small-angle neutron scattering. *Colloids Surf.* **2003**, *213*, 175–187.

(48) Alexandridis, P.; Holzwarth, J. F. Differential Scanning Calorimetry Investigation of the Effect of Salts on Aqueous Solution Properties of an Amphiphilic Block Copolymer (Poloxamer). *Langmuir* **1997**, *13*, 6074–6082.

(49) McCauley, P. J.; Kumar, S.; Calabrese, M. A. Criteria Governing Rod Formation and Growth in Nonionic Polymer Micelles. *Langmuir* **2021**, *37*, 11676–11687.

(50) Vshivkov, S. A.; Zhernov, I. V.; Nadol'skii, A. L.; Mizyov, A. S. Effect of magnetic field on phase transitions in solutions and melts of flexible polymers. *Polym. Sci. - A* **2017**, *59*, 465–472.

(51) Vshivkov, S. A.; Rusinova, E. V.; Klyuzhin, E. S.; Kapitanov, A. A. Effect of Magnetic Field

on Phase Transitions and Structure of Polyelectrolyte Solutions. *Polym. Sci. - A* **2020**, *62*, 62–69.

(52) Alexandridis, P.; Holzwarth, J. F.; Hatton, T. A. Micellization of poly (ethylene oxide)-poly (propylene oxide)-poly (ethylene oxide) triblock copolymers in aqueous solutions: thermodynamics of copolymer association. *Macromolecules* **1994**, *27*, 2414–2425.

(53) Alexandridis, P.; Zhou, D.; Khan, A. Lyotropic Liquid Crystallinity in Amphiphilic Block Copolymers: Temperature Effects on Phase Behavior and Structure for Poly(ethylene oxide)-b-poly(propylene oxide)-b-poly(ethylene oxide) Copolymers of Different Composition. *Langmuir* **1996**, *12*, 2690–2700.

(54) Khalid Hossain, M.; Hinata, S.; Lopez-Quintela, A.; Kunieda, H. Phase Behavior of Poly(Oxyethylene)–Poly(Oxypropylene)–Poly(Oxyethylene) Block Copolymer in Water and Water–C12EO5 Systems. *J. Dispers. Sci. Technol.* **2003**, *24*, 411–422.

(55) Kossuth, M.; Morse, D.; Bates, F. Viscoelastic behavior of cubic phases in block copolymer melts. *J. Rheol.* **1999**, *43*, 167–196.

(56) Booth, C.; Attwood, D. Effects of block architecture and composition on the association properties of poly (oxyalkylene) copolymers in aqueous solution. *Macromol. Rapid Commun.* **2000**, *21*, 501–527.

(57) Mortensen, K.; Pedersen, J. S. Structural study on the micelle formation of poly(ethylene oxide)-poly(propylene oxide)-poly(ethylene oxide) triblock copolymer in aqueous solution. *Macromolecules* **1993**, *26*, 805–812.

(58) Sturcova, A.; Schmidt, P.; Dybal, J. Role of hydration and water coordination in micellization of Pluronic block copolymers. *J. Colloid Interface Sci.* **2010**, *352*, 415–423.

(59) Brubach, J.-B.; Mermet, A.; Filabozzi, A.; Gerschel, A.; Lairez, D.; Krafft, M. P.; Roy, P.

Dependence of Water Dynamics upon Confinement Size. *J. Phys. Chem. B* **2001**, *105*, 430–435.

(60) Calabrò, E.; Magazù, S. Demicellization of polyethylene oxide in water solution under static magnetic field exposure studied by wang spectroscopy. *Adv. Phys. Chem.* **2013**, *2013*.

(61) Brubach, J.-B.; Mermet, A.; Filabozzi, A.; Gerschel, A.; Roy, P. Signatures of the hydrogen bonding in the infrared bands of water. *J. Chem. Phys.* **2005**, *122*, 184509.

(62) Neal, C. A.; Kresge, G. V.; Quan, M. C.; León, V.; Chibambo, N. O.; Calabrese, M. A. Effect of nanoparticle loading and magnetic field application on the thermodynamic, optical, and rheological behavior of thermoresponsive polymer solutions. *J. Vinyl Addit. Technol.* **2022**,

(63) Toledo, E. J.; Ramalho, T. C.; Magriotis, Z. M. Influence of magnetic field on physical–chemical properties of the liquid water: Insights from experimental and theoretical models. *J. Mol. Struct.* **2008**, *888*, 409–415.

(64) Park, M. J.; Bang, J.; Harada, T.; Char, K.; Lodge, T. P. Epitaxial transitions among FCC, HCP, BCC, and cylinder phases in a block copolymer solution. *Macromolecules* **2004**, *37*, 9064–9075.

(65) Park, M. J.; Char, K.; Bang, J.; Lodge, T. P. Interplay between cubic and hexagonal phases in block copolymer solutions. *Langmuir* **2005**, *21*, 1403–1411.

(66) Hanley, K. J.; Lodge, T. P. Effect of dilution on a block copolymer in the complex phase window. *J. Polym. Sci. B Polym. Phys.* **1998**, *36*, 3101–3113.

(67) Hanley, K. J.; Lodge, T. P.; Huang, C.-I. Phase behavior of a block copolymer in solvents of varying selectivity. *Macromolecules* **2000**, *33*, 5918–5931.

(68) Newby, G. E.; Hamley, I. W.; King, S. M.; Martin, C. M.; Terrill, N. J. Structure, rheology and shear alignment of Pluronic block copolymer mixtures. *J. Colloid Interface Sci.* **2009**, *329*, 54–61.

(69) Mortensen, K.; Batsberg, W.; Hvidt, S. Effects of PEO-PPO Diblock Impurities on the Cubic Structure of Aqueous PEO-PPO-PEO Pluronics Micelles: fcc and bcc Ordered Structures in F127. *Macromolecules* **2008**, *41*, 1720–1727.

(70) Gopinadhan, M.; Osuji, C. O. In *Encyclopedia of Polymeric Nanomaterials*; Kobayashi, S., Mullen, K., Eds.; Springer Berlin Heidelberg: Berlin, Heidelberg, 2014; pp 1–10.

(71) Gopinadhan, M.; Majewski, P. W.; Osuji, C. O. Facile alignment of amorphous poly (ethylene oxide) microdomains in a liquid crystalline block copolymer using magnetic fields: Toward ordered electrolyte membranes. *Macromolecules* **2010**, *43*, 3286–3293.

(72) Majewski, P. W.; Gopinadhan, M.; Jang, W.-S.; Lutkenhaus, J. L.; Osuji, C. O. Anisotropic ionic conductivity in block copolymer membranes by magnetic field alignment. *J. Am. Chem. Soc.* **2010**, *132*, 17516–17522.

(73) Gopinadhan, M.; Majewski, P. W.; Choo, Y.; Osuji, C. O. Order-disorder transition and alignment dynamics of a block copolymer under high magnetic fields by in situ x-ray scattering. *Phys. Rev. Lett.* **2013**, *110*, 078301.

(74) He, W.-N.; Xu, J.-T. Crystallization assisted self-assembly of semicrystalline block copolymers. *Prog. Polym. Sci.* **2012**, *37*, 1350–1400.

(75) Zhou, Y.; Ahn, S.-k.; Lakhman, R. K.; Gopinadhan, M.; Osuji, C. O.; Kasi, R. M. Tailoring crystallization behavior of PEO-based liquid crystalline block copolymers through variation in liquid crystalline content. *Macromolecules* **2011**, *44*, 3924–3934.

(76) Vshivkov, S.; Rusinova, E. Effect of magnetic field on phase transitions in solutions of cellulose derivatives. *Polym. Sci. Ser. A* **2008**, *50*, 725–732.

(77) Holysz, L.; Szczes, A.; Chibowski, E. Effects of a static magnetic field on water and electrolyte solutions. *J. Colloid Interface Sci.* **2007**, *316*, 996–1002.

(78) Wang, Y.; Wei, H.; Li, Z. Effect of magnetic field on the physical properties of water. *Results Phys.* **2018**, *8*, 262–267.

(79) Amiri, M. C.; Dadkhah, A. A. On reduction in the surface tension of water due to magnetic treatment. *Coll. Surf. A Physicochem. Eng. Asp.* **2006**, *1*, 252–255.

(80) Cai, R.; Yang, H.; He, J.; Zhu, W. The effects of magnetic fields on water molecular hydrogen bonds. *J. Mol. Struct.* **2009**, *938*, 15–19.

(81) Chang, K.-T.; Weng, C.-I. The effect of an external magnetic field on the structure of liquid water using molecular dynamics simulation. *J. Appl. Phys.* **2006**, *100*, 043917.

(82) Hosoda, H.; Mori, H.; Sogoshi, N.; Nagasawa, A.; Nakabayashi, S. Refractive indices of water and aqueous electrolyte solutions under high magnetic fields. *J. Phys. Chem. A* **2004**, *108*, 1461–1464.

(83) Zhou, K.; Lu, G.; Zhou, Q.; Song, J.; Jiang, S.; Xia, H. Monte Carlo simulation of liquid water in a magnetic field. *J. Appl. Phys.* **2000**, *88*, 1802–1805.

(84) Wang, Q.; Li, L.; Chen, G.; Yang, Y. Effects of magnetic field on the sol-gel transition of methylcellulose in water. *Carbohydr. Polym.* **2007**, *70*, 345–349.

(85) Liu, S.; Li, L. Molecular interactions between PEO–PPO–PEO and PPO–PEO–PPO triblock copolymers in aqueous solution. *Colloids Surf. A: Physicochem. Eng. Asp.* **2015**, *484*, 485–497.

(86) Li, L.; Lim, L. H.; Wang, Q.; Jiang, S. P. Thermoreversible micellization and gelation of a blend of pluronic polymers. *Polymer* **2008**, *49*, 1952–1960.

(87) Kadam, Y.; Ganguly, R.; Kumbhakar, M.; Aswal, V.; Hassan, P.; Bahadur, P. Time dependent sphere-to-rod growth of the Pluronic micelles: Investigating the role of core and corona solvation in determining the micellar growth rate. *J. Phys. Chem. B* **2009**, *113*, 16296–16302.

(88) Ãlvarez Ramirez, J. G.; Fernandez, V. V. A.; Macias, E. R.; Rharbi, Y.; Taboada, P.; Gamez-Corrales, R.; Puig, J. E.; Soltero, J. F. A. Phase behavior of the Pluronic P103/water system in the dilute and semi-dilute regimes. *J. Colloid Interface Sci.* **2009**, *333*, 655–662.